

Geophysical Research Letters[®]



RESEARCH LETTER

10.1029/2024GL111464

Key Points:

- P-wave velocity model from dense seismic refraction data reveal the detailed structure of the detachment at the TAG hydrothermal field
- The TAG hydrothermal field is underlain by a detachment fault with a complex 3-D geometry
- Young detachments, such as under TAG, could exhume lower-crustal gabbro despite limited corrugations and a lack of a dome-shaped footwall

Supporting Information:

Supporting Information may be found in the online version of this article.

Correspondence to:

S. Y. Lai,
syll1n21@soton.ac.uk



Citation:

Lai, S.-Y., Bayrakci, G., Murton, B. J., & Minshull, T. A. (2025). Detachment-fault structure beneath the TAG hydrothermal field, mid-Atlantic ridge, revealed from dense wide-angle seismic data. *Geophysical Research Letters*, 52, e2024GL111464. <https://doi.org/10.1029/2024GL111464>

Received 21 JUL 2024

Accepted 4 JAN 2025

Detachment-Fault Structure Beneath the TAG Hydrothermal Field, Mid-Atlantic Ridge, Revealed From Dense Wide-Angle Seismic Data

Szu-Ying Lai^{1,2} , G. Bayrakci², B. J. Murton² , and T. A. Minshull¹

¹School of Ocean and Earth Science, University of Southampton, National Oceanography Centre Southampton, Southampton, UK, ²National Oceanography Centre, Southampton, UK

Abstract The Trans-Atlantic Geotraverse (TAG) field on the Mid-Atlantic Ridge is one of the largest currently active seafloor hydrothermal fields known. An underlying detachment is inferred to maintain TAG's long-lived hydrothermal discharge, but the detachment lacks a widespread corrugated surface. We used dense wide-angle seismic data to define TAG's detachment structure at a finer scale than has previously been possible. We generated two P-wave velocity profiles of the shallow section of the detachment using first-arrival travel-time tomography, preconditioned by downward continuation. Our results reveal a low-angle detachment, dipping at $\sim 15^\circ$ ($\pm 5^\circ$) at 5 km east of the ridge axis, and evidence for uplifted lower-crustal gabbro in the footwall. Increasing footwall velocities southward suggest a more intense exhumation of deep-seated rocks, showing the detachment's geometry changes along the ridge axis. We conclude the detachment is a complex 3-D structure, and a young system without a dome-shaped footwall can exhumes deep-seated crustal rocks.

Plain Language Summary Hydrothermal vents, where seawater is superheated by magma and discharges mineral-rich fluids through the seafloor, help regulate global ocean chemistry and are a potential resource for base metals. The Trans-Atlantic Geotraverse (TAG) field on the Mid-Atlantic Ridge is one of the largest known deep-sea hydrothermal systems. A long-lived extensional fault, called an oceanic detachment, is believed to localize hydrothermal circulation and venting off the ridge axis. However, current knowledge is still limited on the 3-D geometry of the underlying detachment and how it influences high-temperature hydrothermal activity. We present active-source seismic data to characterize the detachment's subseafloor structure and properties at TAG, where no widespread seafloor outcrop of the fault surface is observed. Our results reveal lower crustal rocks are uplifted by the detachment, with possibly more intense fault deformation to the south of the TAG field. We suggest that the TAG detachment is a young system and expresses variable geometry along strike, with a series of concurrent faults to the north merging into one main fault dominating the south. This observation indicates detachments are complex 3-D structures and even a young detachment lacking a clear exposed fault surface, can accommodate significant tectonic displacement and uplift of deep-seated lithologies.

1. Introduction

The interplay between magmatism and faulting during seafloor spreading shapes the morphology of mid-ocean ridges. At slow-spreading ridges with limited melt supply, oceanic detachment plays a key role in accommodating asymmetric seafloor separation (Cannat, 1993; Dick et al., 2008; Gente et al., 1995) and in maintaining off-axis high-temperature hydrothermal circulation (McCaig et al., 2010). Detachment can account for crustal accretion for 1 and 2 Ma by exhuming lower-crustal and mantle rocks in a domal footwall on the seafloor known as an oceanic core complex (OCC; Cann et al., 1997; Cannat et al., 2006; Smith et al., 2006; Tucholke et al., 1998). An OCC is typically 15–30 km in size with its domed massif marked by spreading-parallel corrugations, thought to indicate the fault slip direction (Cann et al., 2015). Detachments associated with OCCs often show a heterogeneous seismic velocity structure with kilometer-scale spatial variation in dominant lithologies (Canales et al., 2008; Collins et al., 2009; Dunn et al., 2017). This variation is due to the presence of diverse assemblages of eruptive, plutonic, or mantle-derived ultramafic rocks that are highly altered and deformed (Canales et al., 2008; Macleod et al., 2002).

Detachment faults have been considered to initiate with steep dips that then rotate to low angle in a “rolling hinge,” during sequential fault displacement (Buck, 1988; Choi et al., 2013; Reston & Perez-Gussinye, 2007). Paleomagnetic studies support the interpretation of flexural footwall rotation of $\sim 50^\circ$ – 80° that rotates the steep

© 2025. The Author(s).

This is an open access article under the terms of the [Creative Commons Attribution License](https://creativecommons.org/licenses/by/4.0/), which permits use, distribution and reproduction in any medium, provided the original work is properly cited.

detachment to a shallower dip during exhumation and formation of OCC (Garcés & Gee, 2007; MacLeod et al., 2011).

To better understand the evolution of detachments, a thorough study of their sub-seafloor structure is critical. The breakaway, where the detachment initially nucleated, and its emergence, where the corrugated surface of the footwall meets the hanging wall, can be used to estimate the fault dip below the seabed (e.g., De Martin et al., 2007). Yet the nature and geometry of near-surface detachments remain poorly constrained, mostly due to a lack of continuous seismic images of OCCs and their sub-seafloor detachments. This gap has led to competing hypotheses for the along-ridge-axis extent of detachments along the Mid-Atlantic Ridge (MAR). Some advocate a local-scale model in which detachments are controlled by local magma supply, and have a limited along-axis extent, connected by short-offset faults (Smith et al., 2008; Tian & Choi, 2017). Alternatively, the segment-scale model proposes along-strike continuous detachments underlie whole ridge segments, while their fault surfaces can be covered by mass-wasting deposits or aprons that comprise hanging-wall-materials such as unconsolidated volcanics (Olive et al., 2019; T. J. Reston & Ranero, 2011).

Most detachments along the MAR have been known to host active or extinct hydrothermal deposits, implying a link between the detachment faulting and the fluid circulation sustaining the hydrothermal system and their associated seafloor massive sulphide deposits (SMS) (e.g., Andreani et al., 2014; Escartin et al., 2017; Petersen et al., 2009). Hydrothermal systems and SMS deposits are crucial for Earth's biogeochemical exchange and for future metal supply (Hannington et al., 2011). Fractures within detachment can potentially provide fluid pathways for enhanced hydrothermal circulation (Cannat et al., 1991). Therefore, locations of off-axis hydrothermal vents appear dependent on the life cycle of detachments (Gràcia et al., 2000).

The TAG hydrothermal field is one of the largest known seafloor hydrothermal systems, located at 26°N on the TAG segment, 3 and 4 km east of the neo-volcanic axis in the axial valley of the slow-spreading MAR. TAG is a basalt-hosted detachment and hanging-wall hydrothermal system, unlike most MAR hydrothermal vents which sit on the footwall (e.g., Rainbow, Semenov and Logatchev; Canales et al., 2007; Schouten et al., 2010; Smith et al., 2008). At least 15 SMS deposits have been identified here (Murton et al., 2019; Rona et al., 1993), with one active TAG mound, discharging fluids at ~360°C (Campbell et al., 1988; Chiba et al., 2001). Hydrothermal activity in the TAG field has lasted ~150 kyr, albeit intermittently (Lalou et al., 1995) and has generated ~20 Mt of massive sulphides (Graber et al., 2020). Rock drill samples down to 12.5 m below seabed from the Southern mound and the Mir zone (location shown in Figure 1a) show high mineral concentrations, confirming their hydrothermal origins (Murton et al., 2019).

The 40-km-long TAG segment shows a pronounced asymmetry at the segment center, with a more elevated topography east of the axial valley than the west. The eastern ridge flank is comprised of three ridges, where a few gabbro outcrops in fault scarps on the axial-valley wall indicate that vertical movement along the detachment was sufficient to exhume lower-crustal rocks (Figure 1a; Zonenshain et al., 1989). The axial valley hosts a 4 km-wide neo-volcanic zone of hummocky volcanic ridges and young lavas (White et al., 1998). Crustal accretion in this area appears dominated by tectonic extension and magmatism, characterized by dense normal faulting, and dyke eruptions (Humphris & Kleinrock, 1996).

The TAG segment is likely undergoing active detachment faulting. Micro-earthquake data reported the presence of a ~70°-dipping footwall near its root at >7 km depth, then flattening to ~20° at a shallow depth (De Martin et al., 2007). Seismic reflection data imaged a low-angle detachment that was traced up to a potential breakaway at the bathymetric high (Szitkar et al., 2019). A second, recently initiated detachment is proposed by Szitkar et al. (2019) at the Shimmering Hill, with its footwall made of deep-crustal rocks based on magnetic data and microgabbro samples (Figure 1a). Zhao et al. (2012) suggested that the detachment extends 15 km east of the ridge axis to beneath the eastern ridges and has been active for at least 1.35 Myr. This age is consistent with the old fault deduced from morphological analysis (Schouten et al., 2010; Smith et al., 2008), but contrasts with a young system (0.35 Myr) from deep-towed magnetic data (Tivey et al., 2003).

Graber et al. (2020) determine the detachment emergence as a sharp slope break from high-resolution AUV bathymetry (Figures 1a and 1c: blue line), whereas the breakaway is identified with greater uncertainty at a fault scarp that bounds the corrugated surface, suggesting the actual breakaway could be further east (Graber et al., 2020). The TAG detachment seems to lack widespread corrugations or a domed structure typical of OCCs on the MAR such as the Atlantis Massif and Kane OCC (Blackman et al., 1998; Escartin et al., 2003; MacLeod

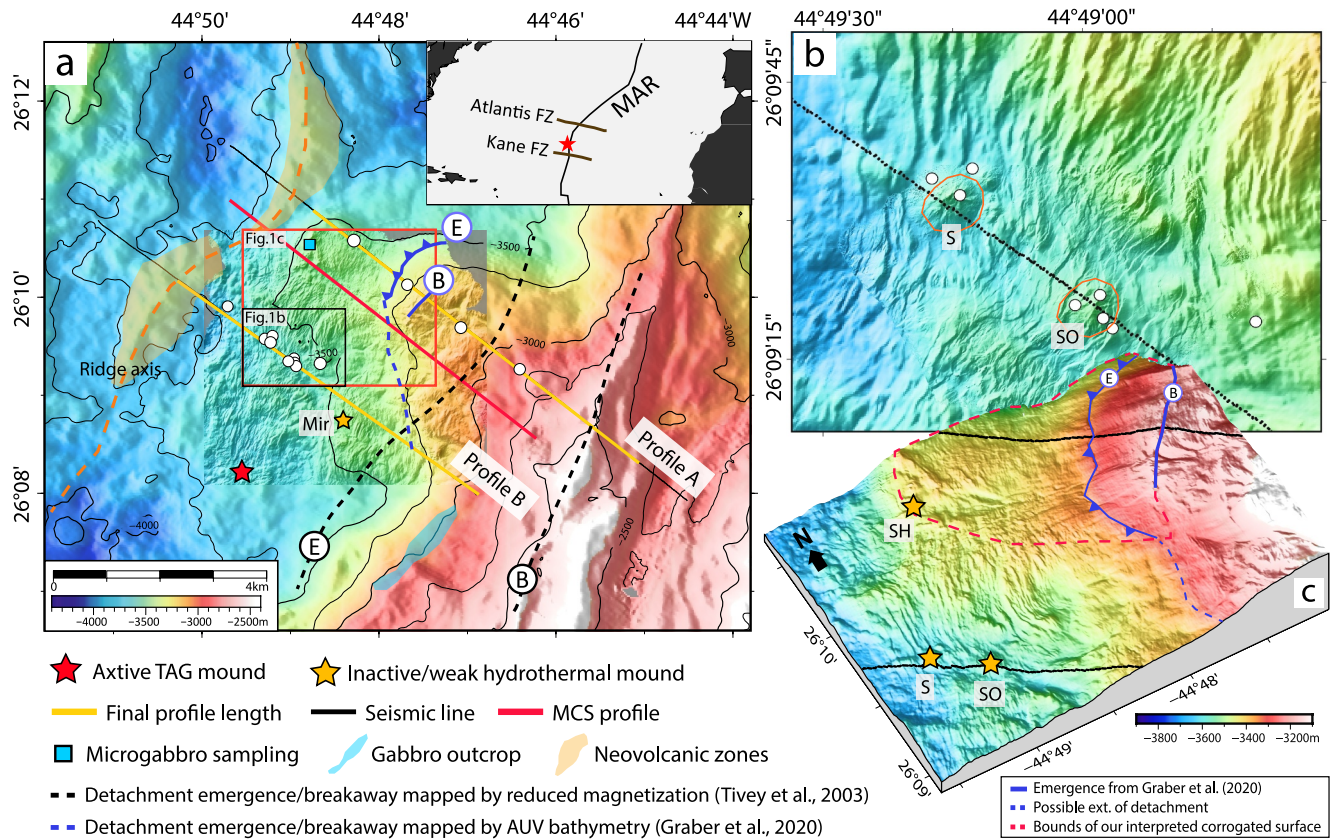


Figure 1. (a) Bathymetry of the TAG hydrothermal field (shipboard 30-m resolution overlain with AUV 2-m resolution) and seismic profiles (black lines). Yellow lines are the final tomographic profiles. Inset shows TAG's location between the Atlantis Fracture Zone (30°N) and the Kane Fracture Zone (24°N). White dots are OBS/OBHs used for tomography. The contours show the water depth every 250 m. Blue square: Seafloor samples of microgabbro at the Shimmering Hill (Sztikar et al., 2019). Blue shading: Gabbro outcrop found at the axial-valley wall (Zonenshain et al., 1989). Black and blue dashed lines labeled E and B show respectively the emergence and breakaway of the detachment identified from magnetic data (Tivey et al., 2003) and AUV bathymetry (Graber et al., 2020). (b) Bathymetry (50-cm resolution) of the Shinkai (S) and Southern (SO) mounds. Note the color scale is different from panel (a) to highlight the mounds. (c) 3-D perspective bathymetry of the red frame from panel (1a). We interpret the corrugated surface (pink dashed line) as extending further seawards to the Shimmering Hill, which hosts the Shimmering mound (SH), than in Graber's (2020, blue line) result. Black lines are seismic profiles.

et al., 2009). Tivey et al. (2003) observed a magnetization low east of the axial valley, which they attributed to crustal thinning by extension along the detachment. They inferred that the bounds of the magnetic-low area mark the bounds of the exposed detachment, that is, the breakaway and emergence. Uncertainties regarding the extent of detachment surface mean that the duration and evolution of the detachment remain unclear, as does its influence on hydrothermal circulation and SMS mineralization (Humphris et al., 2015; McCaig et al., 2010).

In this study, we investigate the nature and geometry of the TAG detachment at depth by resolving its seismic velocity structure using high-resolution wide-angle refraction data. To better define the shallow crustal velocities, we preconditioned the data with downward continuation, a process that moves sources and/or receivers from the acquisition surface to a new, virtual datum in the subsurface and which is commonly used in MCS data to improve velocity determination in the shallow subsurface but has, to date, rarely been applied to ocean-bottom seismic data. Our results reveal previously unresolved variations in velocities at the detachment. We provide new constraints on the 3-D detachment geometry, lithology, and age, and explore its link to magmatism and hydrothermal activity.

2. Data and Methods

2.1. Data Acquisition and Processing

The wide-angle seismic data were collected in 2016 with shots fired every 12 s, giving a nominal spacing of 18 m with a G-gun array of two guns of 6 L each. We focus on two profiles, A and B, each 7 km long, crossing the

detachment (Figure 1a). The profiles stretch from the axial valley to the axial-valley wall, with ~ 1 km of topography change along the profiles. Profile B crosses the Shinkai and the Southern mounds (Figure 1b). Four ocean-bottom hydrophones (OBHs) were deployed every 1 km along profile A, and nine four-component ocean-bottom seismometers (OBSs) along B around the two SMS mounds. Multi-channel seismic reflection (MCS) data were collected concurrently by a 192-channel streamer at 12.5 m group spacing. We included an MCS profile from Sztikar et al. (2019) to complement the imaging of the detachment.

We inverted the refracted first-arrival travel times to build a P-wave velocity (V_p) model. To enhance refraction signals, we applied minimum-phase band-pass filters of 5–8–50–70 Hz at shorter offsets and 2–4–15–25 Hz at longer offsets. First arrivals were then picked on hydrophone and vertical geophone gathers (see Supporting Information S1). We considered two sources of travel-time uncertainty. First, we assigned picking errors based on the S/N ratio at different offsets, informed by picking twice. Second, we considered the travel-time differences for off-line OBSs for the nature of two-dimensional (2-D) travel-time tomography. We projected OBSs onto a 2-D line to respect the true source-receiver offsets (Zelt & Forsyth, 1994). The final travel-time uncertainties range from 12 to 30 ms.

2.2. Downward Continuation

The average water depth of 3.6 km at the TAG hydrothermal field causes near-offset refractions to arrive after the direct water arrivals. For our data, with a maximum offset of 6 km, this delay renders picking most refracted arrivals from the uppermost crust challenging. To improve the ray coverage of shallow turning rays during travel-time inversion, we applied an approach, called downward continuation, which simulates what would be recorded with shots at depth. Downward continuation is a wave-equation process to remove the effect of the water column (e.g., Arnulf et al., 2014; Berryhill, 1979). This processing is often used in MCS data to extract refractions as first arrivals (e.g., Jimenez-Tejero et al., 2022) and less frequently for OBS data (e.g., Zhu et al., 2020). Here, we adapted the processing flow and tested its applicability for our wide-angle OBS data. We extrapolated the shots to a datum close to the seafloor, using a water velocity of 1,500 m/s. After downward continuation, for example, at OBS01 from profile B, the offset of crustal refractions as first arrivals reduced from 2.8 km to as near as 0.8 km. See Supporting Information S1 for more details.

2.3. Travel-Time Tomography

We performed first-arrival travel-time tomography using Tomo2D code (Korenaga et al., 2000) to build the velocity model. A total of 1481 and 2073 travel-time picks were made for profiles A and B respectively (from non-downward-continued data and downward-continued data). Tomo2D first calculates travel times by tracing rays between sources and receivers from the starting model based on the shortest ray path (Moser, 1991) and the ray bending approach (Moser et al., 1992). The linearized inverse problem is then solved to minimize the root-mean-square (RMS) travel-time misfits between the observed and modeled data in a least-squares sense. The starting model is modified iteratively until the RMS misfit is in the order of the uncertainty ($\chi^2 \sim 1$).

To obtain a stable starting model, we smoothed velocities extracted along both profiles from Zhao et al.'s 3-D velocity model (2012). We extracted the seafloor topography from the 30-m and 2-m resolution bathymetry. The model space follows the seabed and extends to 3 km below the seabed. The horizontal grid spacing is 50 m and the vertical spacing is 25–50 m. Model regularization prevents excessive model perturbation during tomography and thus generates a geologically reasonable velocity model. In Tomo2D, regularization is parameterized as a correlation length. We tested the correlation lengths to obtain a model with good ray coverage and ray penetration, without strong small-scale velocity variations, and with a good fit to the observed data. Our chosen horizontal correlation length is 450 m and the vertical correlation length is 250 m. The best-fitting model has an RMS misfit of 17 ms and a χ^2 of 0.9 for profile A (initial RMS misfit of 64 ms) and an RMS misfit of 43 ms and a χ^2 of 0.8 for profile B (initial RMS misfit of 82 ms) (Figure S4 in Supporting Information S1).

3. Results

Our velocity models (Figure 2) reveal the subsurface structure within the upper 1 km of the detachment. Ray coverage is represented by the derivative weight sum (DWS) and is used to mask the model to show regions

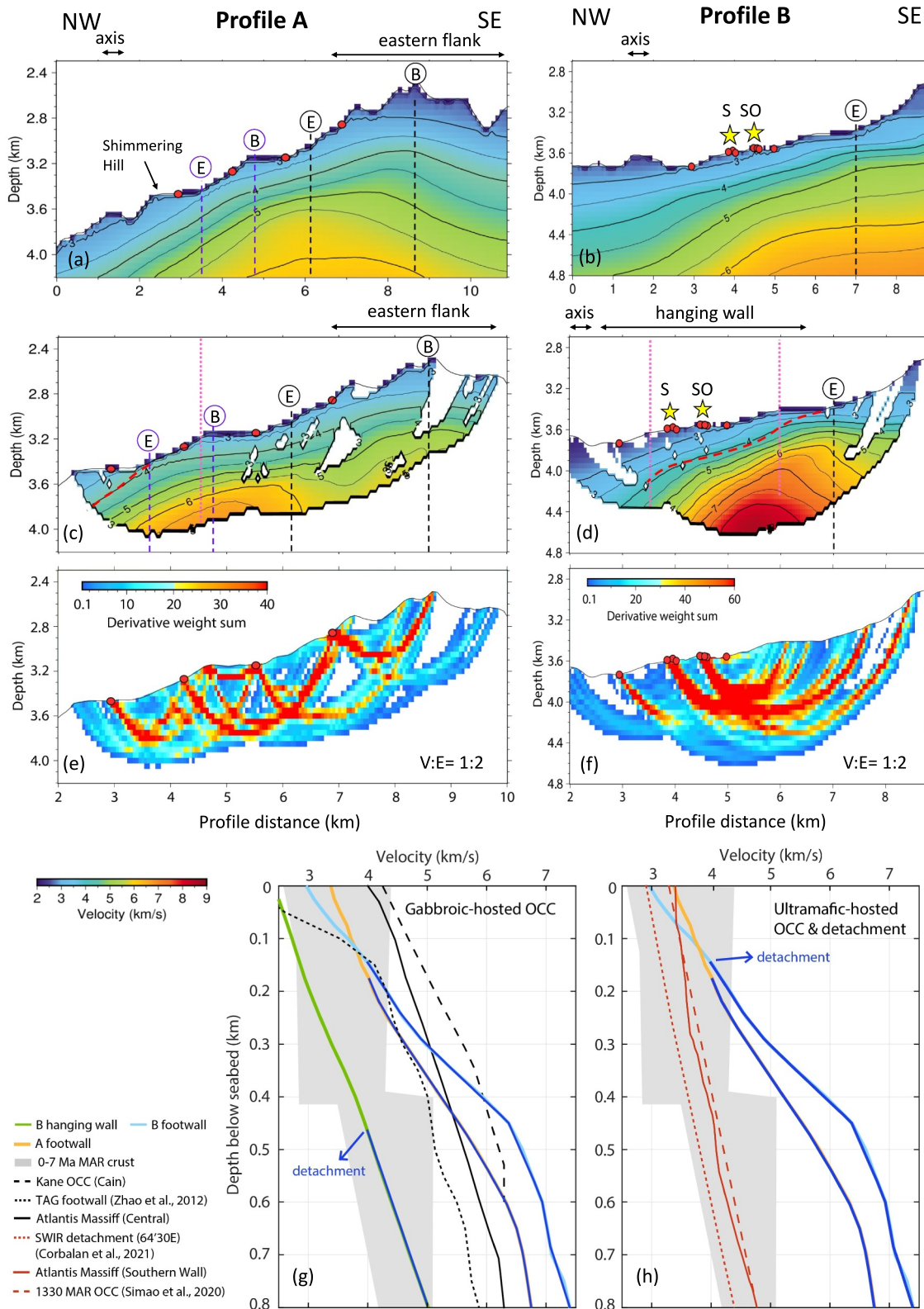


Figure 2.

sampled by the data. DWS provides a good check for model robustness. For both profiles, the well-sampled area reaches 600–700 m below seabed between 3 and 7 km profile distance.

Both profiles show velocities larger than 2.5 km/s and generally higher than the starting models by up to 1.5 km/s (Figure 2). Profile A is characterized by a notable 2.5-km-wide high-velocity region of >6 km/s as shallow as 550 m depth below seabed. This increased velocity is beneath the corrugated surface reported by Graber et al. (2020), likely suggesting the presence of uplifted deep-crustal materials during detachment footwall rotation. Profile B shows a higher velocity gradient toward the east, away from the ridge axis, with velocities increasing from 3 to 7 km/s in a 600 m depth interval (Figures 2d and 2g). Velocities >6 km/s are found at subseafloor depths greater than 400 m. We interpret this velocity structure in profile B to be a result of the detachment faulting, with the detachment dipping toward the ridge axis and extending up to the bathymetric high at ~6.8 km profile distance, which agrees with the emergence reported by Tivey et al. (2003). This high-velocity feature therefore represents the uplifted detachment footwall. The hanging wall has crustal velocities ranging from 2.5 to 4 km/s in the depth range imaged. No corrugations have been identified near profile B from bathymetry despite the west-dipping structure observed in the model. No localized velocity anomaly is resolved beneath the Shinkai and Southern mounds.

To examine the robustness and resolution of our inversion, we performed two tests (a) a restoring resolution test and (b) a checkerboard test (See Text S2 in Supporting Information S1). We added a checkerboard pattern with $\pm 5\%$ of starting model velocities in different sized cells to assess the model's spatial resolution. The checkerboard test shows that our inverted models can resolve feature of 2 and 3 km horizontally (Figures S6 and S7 in Supporting Information S1), sufficient to image the elevated velocity structure associated with the detachment. The inverted model from restoring resolution tests shows a similar velocity feature as the original models, and the lower footwall velocity in Profile A is recovered (Figures S5 and S6 in Supporting Information S1). The resolution tests show that the main detachment structure and north-south variation of footwall velocities are reliably resolved in our models.

4. Discussion

4.1. Lithology and Fault Dip of the TAG Detachment

A shallow west-dipping detachment is clearly revealed in our velocity structures. We mapped the detachment in our models at the 4 km/s velocity contour (Figure 2, red dashed lines) inferred by correlating with a nearby MCS profile (red line in Figure 1a). To correlate seismic velocities with lithology, we extracted 1-D velocity-depth profiles from our models at both hanging wall and footwall to compare with other ultramafic detachments and well-developed OCCs with confirmed in situ geology on the MAR (Figure 2). The hanging wall of the TAG detachment may predominantly consist of neo-volcanics represented by the lower velocities ranging from 2.5 to 4 km/s in profile B (Figure 2d), which correspond to the 0–7 Ma MAR crustal velocities (White et al., 1992). A basaltic hanging wall is consistent with the recovery of highly altered basaltic host rocks at the active TAG mound from ODP Leg 158 (Humphris et al., 1995). The detachment footwall on the other hand shows a significantly higher velocity than the young MAR crust beyond subseafloor depths of 300 m (Figure 2g). The velocity reaches 6.5 km/s at a depth as shallow as 450 m below seabed, suggesting the deeper rocks were uplifted near the surface by detachment faulting.

In general, our footwall velocities are more consistent with the gabbro-dominated Cain Dome at the Kane OCC and with the Atlantis Massif (Figure 2g) than with ultramafic detachments. Over 1.4 km of predominantly gabbroic rocks recovered from IODP Hole U1309D at the Central Dome of the Atlantis Massif provide direct evidence for its gabbroic composition (Blackman et al., 2006). Footwall velocities for both profiles (Figure 2h) are greater than for Southern Ridge, the ultramafic part of the Atlantis Massif with massive outcrops of

Figure 2. Velocity models and comparison of the velocity-depth structure between our results and typical OCCs and detachments. (a, b) Starting model extracted from Zhao et al.'s model (2012). Red circles are OBSs and OBHs. (c, d) Final models masked by DWS. S: Shinkai Mound; SO: Southern Mound. Blue and black dashed lines mark the detachment emergence (E) and breakaway (B) reported from bathymetry (Graber et al., 2020) and magnetic data (Tivey et al., 2003). Red dashed line is the interpreted detachment surface from our results. (e, f) DWS showing the ray coverage through the final models. (g) 1-D velocities compared to Zhao et al. (2012), to young MAR crust (White et al., 1992), and to gabbroic OCCs on the MAR (Canales et al., 2008; Xu et al., 2009). Velocity-depth profiles are extracted from the hanging wall and the footwall through our models. See pink dotted lines in panels c and d for profile locations. (h) 1-D velocities compared to ultramafic detachments at the Southwest Indian Ridge at 64°30'E (Corbalan et al., 2021) and at the 1330 OCC on the MAR (Simao et al., 2020).

serpentinised peridotite (Karson et al., 2006), and for serpentinite detachments at the 1330 OCC on the MAR (Simão et al., 2020) and at the Southwest Indian Ridge (Corbalán et al., 2021). At the TAG hydrothermal field, no ultramafic rocks have been sampled to date, but a few gabbro outcrops were observed at the axial-valley wall (Zonenshain et al., 1989, Figure 1a). Considering these observations together, the TAG detachment footwall is unlikely to contain a large proportion of serpentinised mantle rocks. We infer that gabbroic rocks dominate the footwall at least within the upper 800 m. Our results support the presence of lower-crustal mafic bodies uplifted by the active detachment (Canales et al., 2007; Zhao et al., 2012), which are represented by high velocities in both profiles (Figures 2c and 2d).

In the shallow part of the TAG detachment, we estimate from profile B and a nearby MCS profile that the detachment dips at $\sim 15^\circ$ ($\pm 5^\circ$) and may break the seafloor at least 5 km east of the neo-volcanic ridge axis, where a bathymetric high marks the emergence (Figure 2d). The elevated velocity is observed to the eastern end of the profile, suggesting the detachment can extend to the axial-valley wall. From the bathymetry, the corrugated surface narrows and disappears toward the south of the TAG field. We consider two possible factors affecting the exposure of corrugations. First, numerical modeling by Olive et al. (2019) suggests that detachments of emergence angle $< \sim 13^\circ$ are prone to extensive blanketing by an apron composed of hanging-wall materials that obscures the corrugations. At TAG, the inferred low angle of the detachment meets Olive et al.'s (2019) criterion. Another possibility is that the detachment surface lies beneath a series of fault blocks (rider blocks) that developed between the emergence and the ridge axis. This type of detachment was proposed by Reston and Ranero (2011) and is reported at the Atlantis Massif. Rider blocks have been found to form on a strong fault. Alteration processes such as serpentinisation of ultramafic rocks reduce fault strength and prevent rider block formation (Reston & Ranero, 2011). Alternatively, basalt and gabbroic fault rocks may be little altered and maintain fault strength, resulting in rider block formation. Our results suggest limited serpentinite is present at least within the upper 800 m of the TAG detachment. As a result, rider blocks sliced from the hanging wall, which may comprise the linear axis-parallel ridges east of the axial valley (Figure 1), could explain the scarce exposure of corrugations.

4.2. 3-D Geometry of the TAG Detachment

Although our models confirm the presence of uplifted lower-crustal rocks, we found that velocities beneath Graber et al. (2020)'s reported corrugated surface in the north profile A are lower than those beneath the footwall in the south profile B and other OCCs of a dominantly gabbroic composition (Figure 2g). The lower footwall velocities may imply that the structure in the north has not experienced as much exhumation during the footwall rotation as in the south. We argue that this difference between the two profiles may reflect a different detachment geometry and activity along the fault strike. As previously suggested (Canales et al., 2007), the TAG detachment cannot be explained by a 2-D model.

We re-analysed the bathymetry and found that the spreading-parallel striations on the corrugated block (Figure 1c) seem to extend ~ 1 km further seawards to the Shimmering Hill than the previously defined emergence (Graber et al., 2020). In the nearby MCS profile (red line in Figure 1a), a smoothly dipping detachment surface (detachment 1) beneath the Shimmering Hill can be traced at ~ 0.3 s two-way travel time (tw) below seafloor. West of the hill, another shallower reflector (green, detachment 2) at ~ 0.1 s twt depth can be traced up to the seabed (Figure 3b). Considering the morphological and MCS data together, we infer that the shallower reflector is likely a new detachment, with its footwall exposed on the seabed next to detachment 1. In this scenario, the detachment pattern matches well the successive faults described in Reston and Ranero's (2011) application of the rolling-hinge model. In our 3-D model (Figure 3c), as identified by Sztikar et al. (2019), two detachments accommodate the crustal extension at the north. Toward the south, only one main detachment dominates the extension, with the detachment surface buried beneath a series of fault blocks. Here, upper mantle rocks may be at a shallower depth than in the north due to a more intense footwall rotation that exhumed deeper rocks during detachment faulting.

In profile B, the detachment appears to break the seafloor ~ 5 km east of the ridge axis, which marks the emergence (Figure 2d), consistent with locations from Tivey et al. (2003). If we use the breakaway at the axial-valley wall inferred from the deep-towed magnetics (Tivey et al., 2003), we can estimate the duration of the detachment from the fault heave of ~ 3 km. Considering the half spreading rate to the east of Mid-Atlantic Ridge is ~ 1.2 cm/yr (Tivey et al., 2003), this detachment is likely to be active since ~ 0.25 Ma. Profile A, on the other hand, suggests an ~ 0.45 Ma old detachment with a heave of ~ 5.5 km, when adopting the bathymetry-derived

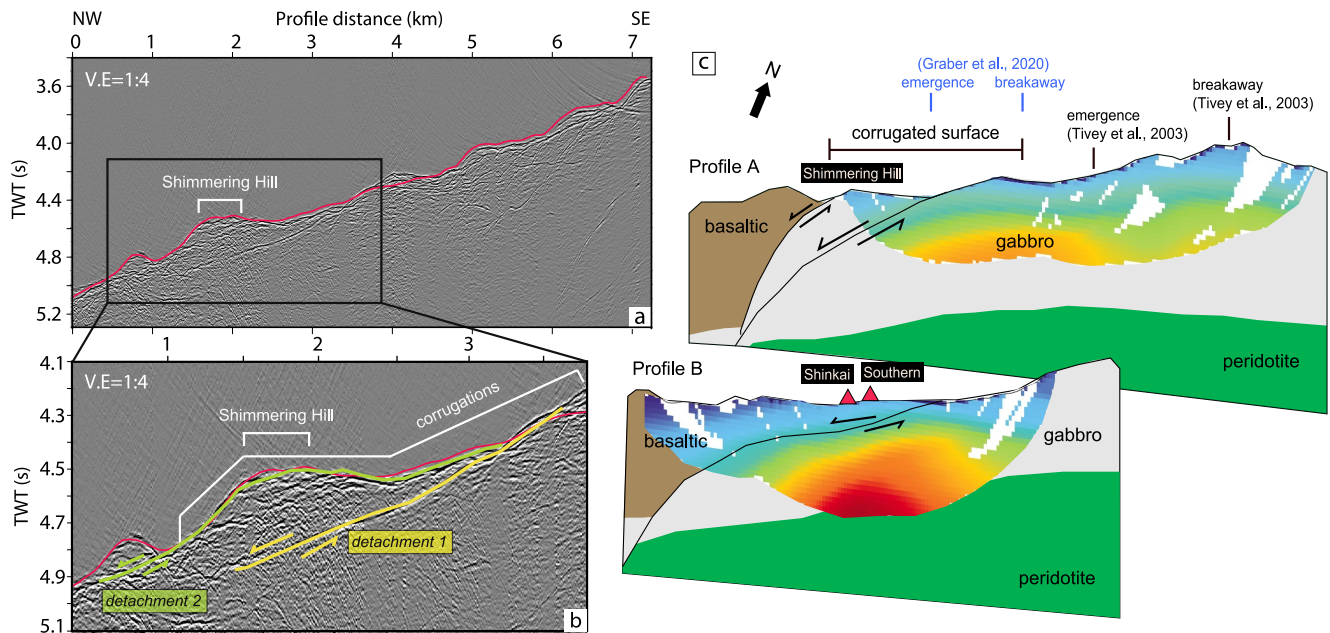


Figure 3. Seismic reflection data (Sztikar et al., 2019; red line in Figure 1a for profile location) and a schematic structural model at the TAG hydrothermal field, showing the 3-D geometry of the detachment. (a) Uninterpreted section. Pink line shows the regional bathymetry. (b) Interpreted section showing the two west-dipping detachment. (c) Low-angle detachment (black line) within the upper 800 m crust was imaged by our velocity models, steepening in the lower crust as imaged from micro-earthquakes by De Martin et al. (2007). Red triangles represent the hydrothermal mounds.

emergence. The younger detachment revealed in profile B than in profile A is not consistent with our observation of a more intense exhumation southward. We therefore suggest that either Tivey et al. (2003)'s breakaway be further eastward, or another detachment is present to the east, as in Zhao et al.'s (2012) model showing that the detachment extends to 15 km east of axis. In this case, the ridge east of the axial valley in Figure 1a could be a fault block marking a breakaway of our imaged detachment, connecting to an older detachment. The TAG detachment in general is a young system, supported by the lack of the OCC feature and widespread corrugations. The abundant SMS deposits (Southern, Shinkai mound, Mir zone, and TAG mound) in the southern part of the TAG hydrothermal field in comparison with the northern area (Graber et al., 2020) imply intense hydrothermal activity at the hanging wall. Although no velocity anomaly is revealed in our models associated with this activity, we speculate that the greater detachment exhumation in the south facilitates the hydrothermal circulation.

5. Conclusions

We generated two P-wave velocity models across the detachment at the TAG segment using first-arrival travel-time tomography of wide-angle seismic data. The application of downward continuation improved the resolution of our velocity models. This technique effectively extracted the near-offset refractions as first arrivals for data acquired with a short offset <5 km at a water depth of 3.6 km. Our results elucidate an asymmetric crustal structure in the upper 800 m of the detachment. The results, together with published outcrop observations, revealed the presence of lower-crustal gabbro in the footwall at a depth as shallow as 400 m uplifted by the detachment, and basaltic volcanics in the hanging wall.

Our results confirm that detachment's geometry can vary along the ridge axis. The tectonic extension at the TAG segment is accommodated by successive detachments in the north and one dominant detachment in the south. More intense exhumation of deep-seated rocks may occur southwards. We suggest that the limited corrugated surface at TAG could be either due to the low emergence angle of the detachment ($15^{\circ} \pm 5^{\circ}$) that causes it to be covered by mass-wasting aprons, or due to burial of the detachment beneath a series of small fault blocks as in the rolling-hinge model. The TAG detachment is a young system, being active for at least ~ 0.45 Ma from our results. Our study shows that the detachment is a complex 3-D structure, and that a young system without the morphology of an OCC can exhume lower-crustal rocks, so extension along detachments may be playing an important role in many areas where OCC morphology is absent.

Data Availability Statement

Wide-angle OBS/OBH and MCS data used in this study from METEOR Cruise M127 are available at Bialas et al. (2020). Bathymetric data from AUV are available at Petersen (2019a). Raw data of the shipboard multibeam bathymetry are available at Petersen (2019b).

Acknowledgments

SYL is funded by the PhD studentship from Equinor to conduct this research at National Oceanography Centre, Southampton. This research is based on seismic data acquired during cruise M127 within the framework of the EU-funded Blue Mining project (<http://bluemining.eu/>) under Grant 604500. We thank the cruise participants and ship crew from Cruise M127 for their hard work in data acquisition. We thank J. Pablo Canales (Woods Hole Oceanographic Institution) for providing the 3-D P-wave tomographic velocity model to support our starting model building. We thank J. Pablo Canales and Matthias Delescluse for their careful and constructive reviews.

References

- Andreani, M., Escartin, J., Delacour, A., Ildefonse, B., Godard, M., Dymont, J., et al. (2014). Tectonic structure, lithology, and hydrothermal signature of the Rainbow massif (Mid-Atlantic Ridge 36°14'N). *Geochemistry, Geophysics, Geosystems*, 15(9), 3543–3571. <https://doi.org/10.1002/2014GC005269>
- Arnulf, A. F., Harding, A. J., Kent, G. M., Singh, S. C., & Crawford, W. C. (2014). Constraints on the shallow velocity structure of the Lucky Strike Volcano, Mid-Atlantic Ridge, from downward continued multichannel streamer data. *Journal of Geophysical Research*, 119(2), 1119–1144. <https://doi.org/10.1002/2013JB010500>
- Berryhill, J. R. (1979). Wave-equation datuming. *Geophysics*, 44(8), 1329–1344. <https://doi.org/10.1190/1.1441010>
- Bialas, J., Dannowski, A., & Murton, B. J. (2020). Ocean bottom seismometer and ocean bottom hydrophone sgy-files of seismic refraction and wide angle data from profiles P01-P46 at TAG hydrothermal field during METEOR cruise M127 with links to data files [Dataset]. PANGAEA. <https://doi.org/10.1594/PANGAEA.914369>
- Blackman, D. K., Cann, J. R., Janssen, B., & Smith, D. K. (1998). Origin of extensional core complexes: Evidence from the mid-Atlantic Ridge at Atlantis fracture zone. *Journal of Geophysical Research*, 103(B9), 21315–21333. <https://doi.org/10.1029/98JB01756>
- Blackman, D. K., Ildefonse, B., John, B. E., Ohara, Y., Miller, D. J., & MacLeod, C. J. (2006). In *Proceedings of IODP*, 304/305. <https://doi.org/10.2204/iodp.proc.304305.2006>
- Buck, W. R. (1988). Flexural rotation of normal faults. *Tectonics*, 7(5), 959–973. <https://doi.org/10.1029/TC007i005p00959>
- Campbell, A. C., Palmer, M. R., Klinkhammer, G. P., Bowers, T. S., Edmond, J. M., Lawrence, J. R., et al. (1988). Chemistry of hot springs on the Mid-Atlantic Ridge. *Nature*, 335(6190), 514–519. <https://doi.org/10.1038/335514a0>
- Canales, J. P., Sohn, R. A., & de Martin, B. J. (2007). Crustal structure of the Trans-Atlantic Geotraverse (TAG) segment (Mid-Atlantic Ridge, 26° 10'N): Implications for the nature of hydrothermal circulation and detachment faulting at slow spreading ridges. *Geochemistry, Geophysics, Geosystems*, 8(8). <https://doi.org/10.1029/2007GC001629>
- Canales, J. P., Tucholke, B. E., Xu, M., Collins, J. A., & DuBois, D. L. (2008). Seismic evidence for large-scale compositional heterogeneity of oceanic core complexes. *Geochemistry, Geophysics, Geosystems*, 9(8). <https://doi.org/10.1029/2008GC002009>
- Cann, J. R., Blackman, D. K., Smith, D. K., McAllister, E., Janssen, B., Mello, S., et al. (1997). Corrugated slip surfaces formed at ridge–transform intersections on the Mid-Atlantic Ridge. *Nature*, 385(6614), 329–332. <https://doi.org/10.1038/385329a0>
- Cann, J. R., Smith, D. K., Escartin, J., & Schouten, H. (2015). Tectonic evolution of 200 km of Mid-Atlantic Ridge over 10 million years: Interplay of volcanism and faulting. *Geochemistry, Geophysics, Geosystems*, 16(7), 2303–2321. <https://doi.org/10.1002/2015GC005797>
- Cannat, M. (1993). Emplacement of mantle rocks in the seafloor at mid-ocean ridges. *Journal of Geophysical Research*, 98(B3), 4163–4172. <https://doi.org/10.1029/92JB02221>
- Cannat, M., Mével, C., & Stakes, D. (1991). Stretching of the deep crust at the slow-spreading Southwest Indian Ridge. *Tectonophysics*, 190(1), 73–94. [https://doi.org/10.1016/0040-1951\(91\)90355-V](https://doi.org/10.1016/0040-1951(91)90355-V)
- Cannat, M., Sauter, D., Mendel, V., Ruellan, E., Okino, K., Escartin, J., et al. (2006). Modes of seafloor generation at a melt-poor ultraslow-spreading ridge. *Geology*, 34(7), 605–608. <https://doi.org/10.1130/G22486.1>
- Chiba, H., Masuda, H., Lee, S. Y., & Fujioka, K. (2001). Chemistry of hydrothermal fluids at the TAG active mound, MAR 26. *Geophysical Research Letters*, 28(15), 2919–2922. <https://doi.org/10.1029/2000GL012645>
- Choi, E., Buck, R., Lavier, L., & Petersen, K. D. (2013). Using core complex geometry to constrain fault strength. *Geophysical Research Letters*, 40(15), 3863–3867. <https://doi.org/10.1002/grl.50732>
- Collins, J. A., Blackman, D. K., Harris, A., & Carlson, R. L. (2009). Seismic and drilling constraints on velocity structure and reflectivity near IODP Hole U1309D on the central dome of Atlantis Massif, Mid-Atlantic Ridge 30°N. *Geochemistry, Geophysics, Geosystems*, 10(1). <https://doi.org/10.1029/2008gc002121>
- Corbalán, A., Nedimović, M. R., Louden, K. E., Cannat, M., Grevemeyer, I., Watremez, L., & Leroy, S. (2021). Seismic velocity structure along and across the ultraslow-spreading southwest Indian Ridge at 64°30'E showcases flipping detachment faults. *Journal of Geophysical Research: Solid Earth*, 126(10). <https://doi.org/10.1029/2021JB022177>
- De Martin, B. J., Reves-Sohn, R. A., Canales, J. P., & Humphris, S. E. (2007). Kinematics and geometry of active detachment faulting beneath the Trans-Atlantic geotraverse (TAG) hydrothermal field on the Mid-Atlantic Ridge. *Geology*, 35(8), 711–714. <https://doi.org/10.1130/G23718A.1>
- Dick, H. J. B., Tivey, M. A., & Tucholke, B. E. (2008). Plutonic foundation of a slow-spreading ridge segment: Oceanic core complex at Kane Megamullion, 23°30'N, 45°20'W. *Geochemistry, Geophysics, Geosystems*, 9(5). <https://doi.org/10.1029/2007GC001645>
- Dunn, R. A., Arai, R., Eason, D. E., Canales, J. P., & Sohn, R. A. (2017). Three-dimensional seismic structure of the mid-Atlantic Ridge: An investigation of tectonic, magmatic, and hydrothermal processes in the rainbow area. *Journal of Geophysical Research: Solid Earth*, 122(12), 9580–9602. <https://doi.org/10.1002/2017JB015051>
- Escartin, J., Mevel, C., MacLeod, C., & McCaig, A. (2003). 24—Constraints on deformation conditions and the origin of oceanic detachments: The Mid-Atlantic Ridge core complex at 15°45'N. *Geochemistry, Geophysics, Geosystems*, 4(8), 1067. <https://doi.org/10.1029/2002gc000472>
- Escartin, J., Mével, C., Petersen, S., Bonnemaïns, D., Cannat, M., Andreani, M., et al. (2017). Tectonic structure, evolution, and the nature of oceanic core complexes and their detachment fault zones (13°20'N and 13°30'N, Mid Atlantic Ridge). *Geochemistry, Geophysics, Geosystems*, 18(4), 1451–1482. <https://doi.org/10.1002/2016GC006775>
- Garcés, M., & Gee, J. S. (2007). Paleomagnetic evidence of large footwall rotations associated with low-angle faults at the Mid-Atlantic Ridge. *Geology*, 35(3), 279. <https://doi.org/10.1130/g23165a.1>
- Gente, P., Pockalny, R. A., Durand, C., Deplus, C., Maia, M., Ceuleneer, G., et al. (1995). EPSL Characteristics and evolution of the segmentation of the mid-Atlantic Ridge between 20°N and 24°N during the last 10 million years. *Earth and Planetary Science Letters*, 129(1–4), 55–71. [https://doi.org/10.1016/0012-821x\(94\)00233-o](https://doi.org/10.1016/0012-821x(94)00233-o)
- Graber, S., Petersen, S., Yeo, I., Sztikar, F., Klischies, M., Jamieson, J., et al. (2020). Structural control, evolution, and accumulation rates of massive sulfides in the TAG hydrothermal field. *Geochemistry, Geophysics, Geosystems*, 21(9). <https://doi.org/10.1029/2020GC009185>

- Gràcia, E., Charlou, J.-L., Knoery, J., & Parson, L. (2000). Non-transform offsets along the Mid-Atlantic Ridge south of the Azores (38°N–34°N): Ultramafic exposures and hosting of hydrothermal vents. *Earth and Planetary Science Letters*, 177(1–2), 89–103. [https://doi.org/10.1016/S0012-821X\(00\)00034-0](https://doi.org/10.1016/S0012-821X(00)00034-0)
- Hannington, M., Jamieson, J., Monecke, T., Petersen, S., & Beaulieu, S. (2011). The abundance of seafloor massive sulfide deposits. *Geology*, 39(12), 1155–1158. <https://doi.org/10.1130/G32468.1>
- Humphris, S. E., Herzig, P. M., Miller, D. J., Alt, J. C., Becker, K., Brown, D., et al. (1995). The internal structure of an active sea-floor massive sulphide deposit. *Nature*, 377(6551), 713–716. <https://doi.org/10.1038/377713a0>
- Humphris, S. E., & Kleinrock, M. C. (1996). Detailed morphology of the TAG active hydrothermal mound: Insights into its formation and growth. *Geophysical Research Letters*, 23(23), 3443–3446. <https://doi.org/10.1029/96GL03079>
- Humphris, S. E., Tivey, M. K., & Tivey, M. A. (2015). The trans-Atlantic geotraverse hydrothermal field: A hydrothermal system on an active detachment fault. *Deep-Sea Research Part II Topical Studies in Oceanography*, 121, 8–16. <https://doi.org/10.1016/j.dsr2.2015.02.015>
- Jimenez-Tejero, C. E., Ranero, C. R., Sallares, V., & Gras, C. (2022). Downward continuation of marine seismic reflection data: An undervalued tool to improve velocity models. *Geophysical Journal International*, 230(2), 831–848. <https://doi.org/10.1093/gji/ggac087>
- Karson, J. A., Früh-Green, G. L., Kelley, D. S., Williams, E. A., Yoerger, D. R., & Jakuba, M. (2006). Detachment shear zone of the Atlantis Massif core complex, Mid-Atlantic Ridge, 30°N. *Geochemistry, Geophysics, Geosystems*, 7(6). <https://doi.org/10.1029/2005GC001109>
- Korenaga, J., Holbrook, W. S., Kent, G. M., Kelemen, P. B., Detrick, R. S., Larsen, H. C., et al. (2000). Crustal structure of the southeast Greenland margin from joint refraction and reflection seismic tomography. *Journal of Geophysical Research*, 105(B9), 21591–21614. <https://doi.org/10.1029/2000jb900188>
- Lalou, C., Reyss, J.-L., Brichet, E., Rona, P. A., & Thompson, G. (1995). Hydrothermal activity on a 105-year scale at a slow-spreading ridge, TAG hydrothermal field, Mid-Atlantic Ridge 26°N. *Journal of Geophysical Research*, 100(B9), 17855–17862. <https://doi.org/10.1029/95jb01858>
- Macleod, C. J., Banerji, D., Banks, G. J., Irving, D. H. B., Lilly, R. M., Mccaig, A. M., & Smith, D. K. (2002). Direct geological evidence for oceanic detachment faulting: The mid-Atlantic Ridge, 1545°N. *Geology*, 30(10), 879–892. [https://doi.org/10.1130/0091-7613\(2002\)030<0879:DGEFOD>2.0.CO;2](https://doi.org/10.1130/0091-7613(2002)030<0879:DGEFOD>2.0.CO;2)
- MacLeod, C. J., Carlut, J., Escartín, J., Horen, H., & Morris, A. (2011). Quantitative constraint on footwall rotations at the 15°45′N oceanic core complex, mid-Atlantic Ridge: Implications for oceanic detachment fault processes. *Geochemistry, Geophysics, Geosystems*, 12(5). <https://doi.org/10.1029/2011GC003503>
- MacLeod, C. J., Searle, R. C., Murton, B. J., Casey, J. F., Mallows, C., Unsworth, S. C., et al. (2009). Life cycle of oceanic core complexes. *Earth and Planetary Science Letters*, 287(3–4), 333–344. <https://doi.org/10.1016/j.epsl.2009.08.016>
- McCaig, A. M., Delacour, A., Fallick, A. E., Castelain, T., & Früh-Green, G. L. (2010). Detachment fault control on hydrothermal circulation systems: Interpreting the subsurface beneath the TAG hydrothermal field using the isotopic and geological evolution of oceanic core complexes in the Atlantic. *Geophysical Monograph Series*, 188, 207–239. <https://doi.org/10.1029/2008GM000729>
- Moser, T. J. (1991). Shortest path calculation of seismic rays. *Geophysics*, 56(1), 59–67. <https://doi.org/10.1190/1.1442958>
- Moser, T. J., Nolet, G., & Snieder, R. (1992). Ray bending revisited. *Bulletin of the Seismological Society of America*, 82(1), 259–288.
- Murton, B. J., Lehrmann, B., Dutrieux, A. M., Martins, S., de la Iglesia, A. G., Stobbs, I. J., et al. (2019). Geological fate of seafloor massive sulphides at the TAG hydrothermal field (Mid-Atlantic Ridge). *Ore Geology Reviews*, 107, 903–925. <https://doi.org/10.1016/j.oregeorev.2019.03.005>
- Olive, J. A., Parnell-Turner, R., Escartín, J., Smith, D. K., & Petersen, S. (2019). Controls on the seafloor exposure of detachment fault surfaces. *Earth and Planetary Science Letters*, 506, 381–387. <https://doi.org/10.1016/j.epsl.2018.11.001>
- Petersen, S. (2019a). Bathymetric data products from AUV dives during METEOR cruise M127 (TAG Hydrothermal Field, Atlantic) [Dataset]. *GEOMAR—Helmholtz Centre for Ocean Research Kiel, PANGAEA*. <https://doi.org/10.1594/PANGAEA.899415>
- Petersen, S. (2019b). Raw multibeam EM122 data and data products: METEOR cruise M127 (TAG Hydrothermal Field, Atlantic) [Dataset]. *GEOMAR—Helmholtz Centre for Ocean Research Kiel, PANGAEA*. <https://doi.org/10.1594/PANGAEA.899408>
- Petersen, S., Kuhn, K., Kuhn, T., Augustin, N., Hékinian, R., Franz, L., & Borowski, C. (2009). The geological setting of the ultramafic-hosted Logatchev hydrothermal field (14°45′N, Mid-Atlantic Ridge) and its influence on massive sulfide formation. *Lithos*, 112(1–2), 40–56. <https://doi.org/10.1016/j.lithos.2009.02.008>
- Reston, T., & Perez-Gussinye, M. (2007). Lithospheric extension from rifting to continental breakup at magma-poor margins: Rheology, serpentinisation and symmetry. *International Journal of Earth Sciences*, 96(6), 1033–1046. <https://doi.org/10.1007/s00531-006-0161-z>
- Reston, T. J., & Ranero, C. R. (2011). The 3-D geometry of detachment faulting at mid-ocean ridges. *Geochemistry, Geophysics, Geosystems*, 12(7). <https://doi.org/10.1029/2011GC003666>
- Rona, P. A., Bogdanov, Y. A., Gurchich, E. G., Rimski-Korsakov, N. A., Sagalevitch, A. M., Hannington, M. D., & Thompson, G. (1993). Relict hydrothermal zones in the TAG hydrothermal field, Mid-Atlantic Ridge 26°N, 45°W. *Journal of Geophysical Research*, 98(B6), 9715–9730. <https://doi.org/10.1029/93JB00552>
- Schouten, H., Smith, D. K., Cann, J. R., & Escartín, J. (2010). Tectonic versus magmatic extension in the presence of core complexes at slow-spreading ridges from a visualization of faulted seafloor topography. *Geology*, 38(7), 615–618. <https://doi.org/10.1130/G30803.1>
- Simão, N. M., Peirce, C., Funnell, M. J., Robinson, A. H., Searle, R. C., Macleod, C. J., & Reston, T. J. (2020). 3-D P-wave velocity structure of oceanic core complexes at 13°N on the Mid-Atlantic Ridge. *Geophysical Journal International*, 221(3), 1555–1579. <https://doi.org/10.1093/gji/ggaa093>
- Smith, D., Cann, J., & Escartín, J. (2006). Widespread active detachment faulting and core complex formation near 13°N on the Mid-Atlantic Ridge. *Nature*, 442(7101), 440–443. <https://doi.org/10.1038/nature04950>
- Smith, D. K., Escartín, J., Schouten, H., & Cann, J. R. (2008). Fault rotation and core complex formation: Significant processes in seafloor formation at slow-spreading mid-ocean ridges (Mid-Atlantic Ridge, 13°–15°N). *Geochemistry, Geophysics, Geosystems*, 9(3). <https://doi.org/10.1029/2007GC001699>
- Szitar, F., Dymant, J., Petersen, S., Bialas, J., Klischies, M., Graber, S., et al. (2019). Detachment tectonics at mid-Atlantic Ridge 26°N. *Scientific Reports*, 9(1), 11830. <https://doi.org/10.1038/s41598-019-47974-z>
- Tian, X., & Choi, E. (2017). Effects of axially variable diking rates on faulting at slow spreading mid-ocean ridges. *Earth and Planetary Science Letters*, 458, 14–21. <https://doi.org/10.1016/j.epsl.2016.10.033>
- Tivey, M. A., Schouten, H., & Kleinrock, M. C. (2003). A near-bottom magnetic survey of the Mid-Atlantic Ridge axis at 26°N: Implications for the tectonic evolution of the TAG segment. *Journal of Geophysical Research*, 108(B5). <https://doi.org/10.1029/2002jb001967>
- Tucholke, B. E., Lin, J., & Kleinrock, M. C. (1998). Megamullions and mullion structure defining oceanic metamorphic core complexes on the Mid-Atlantic Ridge. *Journal of Geophysical Research*, 103(B5), 9857–9866. <https://doi.org/10.1029/98JB00167>

- White, S. N., Humphris, S. E., & Kleinrock, M. C. (1998). New observations on the distribution of past and present hydrothermal activity in the TAG area of the Mid-Atlantic Ridge (26°08' N). *Marine Geophysical Researches*, 20(1), 41–56. <https://doi.org/10.1023/a:1004376229719>
- White, R. S., McKenzie, D., & O'Nions, R. K. (1992). Oceanic crustal thickness from seismic measurements and rare earth element inversions. *Journal of Geophysical Research*, 97(B13), 19683–19715. <https://doi.org/10.1029/92JB01749>
- Xu, M., Canales, J. P., Tucholke, B. E., & DuBois, D. L. (2009). Heterogeneous seismic velocity structure of the upper lithosphere at Kane oceanic core complex, Mid-Atlantic Ridge. *Geochemistry, Geophysics, Geosystems*, 10(10). <https://doi.org/10.1029/2009GC002586>
- Zelt, C. A., & Forsyth, D. A. (1994). Modeling wide-angle seismic data for crustal structure: Southeastern Grenville Province. *Journal of Geophysical Research*, 99(B6), 11687–11704. <https://doi.org/10.1029/93jb02764>
- Zhao, M., Canales, J. P., & Sohn, R. A. (2012). Three-dimensional seismic structure of a Mid-Atlantic Ridge segment characterized by active detachment faulting (Trans-Atlantic Geotraverse, 2555°N–2620°N). *Geochemistry, Geophysics, Geosystems*, 13(1). <https://doi.org/10.1029/2012GC004454>
- Zhu, J., Canales, J. P., Han, S., Carbotte, S. M., Arnulf, A., & Nedimović, M. R. (2020). Vp/Vs ratio of incoming sediments off Cascadia subduction zone from analysis of controlled-source multicomponent OBS records. *Journal of Geophysical Research: Solid Earth*, 125(6), e2019JB019239. <https://doi.org/10.1029/2019JB019239>
- Zonenshain, L. P., Kuzmin, M. I., Lisitsin, A. P., Bogdanov, Y. A., & Baranov, B. V. (1989). Tectonics of the Mid-Atlantic rift valley between the TAG and MARK areas (26–24°N): Evidence for vertical tectonism. *Tectonophysics*, 159(1), 1–23. [https://doi.org/10.1016/0040-1951\(89\)90167-4](https://doi.org/10.1016/0040-1951(89)90167-4)

References From the Supporting Information

- Arnulf, A. F., Singh, S. C., Harding, A. J., Kent, G. M., & Crawford, W. (2011). Strong seismic heterogeneity in layer 2A near hydrothermal vents at the Mid-Atlantic Ridge. *Geophysical Research Letters*, 38(13), L13320. <https://doi.org/10.1029/2011GL047753>
- Humphreys, E., & Clayton, R. W. (1988). Adaptation of back projection tomography to seismic travel time problems. *Journal of Geophysical Research*, 93(B2), 1073–1085. <https://doi.org/10.1029/JB093iB02p01073>
- Zhao, D., Hasegawa, A., & Horiuchi, S. (1992). Tomographic imaging of P and S wave velocity structure beneath northeastern Japan. *Journal of Geophysical Research*, 97(B13), 19909–19928. <https://doi.org/10.1029/92jb00603>